



CHALMERS
UNIVERSITY OF TECHNOLOGY

Fast generation of Schrödinger cat states using a Kerr-tunable superconducting resonator

Downloaded from: <https://research.chalmers.se>, 2023-10-28 13:59 UTC

Citation for the original published paper (version of record):

He, X., Lu, Y., Bao, D. et al (2023). Fast generation of Schrödinger cat states using a Kerr-tunable superconducting resonator. *Nature Communications*, 14(1).
<http://dx.doi.org/10.1038/s41467-023-42057-0>

N.B. When citing this work, cite the original published paper.

Fast generation of Schrödinger cat states using a Kerr-tunable superconducting resonator

Received: 6 April 2023

Accepted: 28 September 2023

Published online: 11 October 2023

 Check for updatesX. L. He^{1,2,7}, Yong Lu^{3,4,7}✉, D. Q. Bao^{1,2}, Hang Xue^{1,2}, W. B. Jiang^{1,2}, Z. Wang^{1,2}, A. F. Roudsari⁴, Per Delsing⁴, J. S. Tsai^{5,6} & Z. R. Lin^{1,2}✉

Schrödinger cat states, quantum superpositions of macroscopically distinct classical states, are an important resource for quantum communication, quantum metrology and quantum computation. Especially, cat states in a phase space protected against phase-flip errors can be used as a logical qubit. However, cat states, normally generated in three-dimensional cavities and/or strong multi-photon drives, are facing the challenges of scalability and controllability. Here, we present a strategy to generate and preserve cat states in a coplanar superconducting circuit by the fast modulation of Kerr nonlinearity. At the Kerr-free work point, our cat states are passively preserved due to the vanishing Kerr effect. We are able to prepare a 2-component cat state in our chip-based device with a fidelity reaching 89.1% under a 96 ns gate time. Our scheme shows an excellent route to constructing a chip-based bosonic quantum processor.

Quantum computation has been proven to surpass classical architectures in certain computational tasks¹. Quantum information has been encoded and manipulated in diverse systems such as cold atoms², trapped ions^{3,4}, superconducting circuits⁵. Especially, superconducting circuit is a promising platform which has shown significant progress on the gate-based quantum computers^{1,6}. Additional qubit elements are normally required to achieve large-scale error-correctable two-level system-based quantum computation⁷. In contrast, the phase space of a bosonic system inherently provides a larger Hilbert space and thus a larger coding area^{8–11}. Therefore, encoding quantum information in continuous variables leads to a significant reduction in hardware overhead on the path towards the fault-tolerance^{12,13}. The nonclassical states with negative Wigner functions^{14,15} can be regarded as a quantum computing resource to obtain quantum computational advantage. Recently, non-classical states including Schrödinger's cat codes¹⁶ binominal codes¹⁷, GKP states^{18,19}, and cubic-phase states^{18,20},

have been demonstrated in cavities coupled to ancillary qubits. However, the ancillary qubit normally has a fixed Kerr nonlinearity which might be detrimental even for the storage of nonclassical state²¹. In previous results, Schrödinger's cat states were mostly generated by engineering the two-photon losses^{22,23} or ancilla-assisted processes²⁴ in two-^{25,26} and three-dimensional²³ structures.

In this paper, differently from traditional gate-based cavity control schemes using the dispersive shift of a nominally linear resonator to an ancilla qubit^{24–26}, our cat state preparation scheme is an alternate by applying a displacement followed by a Kerr gate to a nonlinear resonator. The Kerr gate is implemented by quickly tuning the nonlinearity of the resonator terminated by a Superconducting Nonlinear Asymmetric Inductive eLement (SNAIL)^{27,28} as shown in Fig. 1a. Moreover, by tuning the flux bias to the Kerr-free point with eliminated four-wave mixing term, we therefore preserve the prepared cat states against the Kerr-induced evolution.

¹National Key Laboratory of Materials for Integrated Circuits, Shanghai Institute of Microsystem and Information Technology, Chinese Academy of Sciences, 200050 Shanghai, China. ²University of Chinese Academy of Science, 100049 Beijing, China. ³3rd Physikalisches Institut, University of Stuttgart, 70569 Stuttgart, Germany. ⁴Microtechnology and Nanoscience, Chalmers University of Technology, SE-412 96 Göteborg, Sweden. ⁵Graduate School of Science, Tokyo University of Science, Shinjuku, Tokyo 162-0825, Japan. ⁶Center for Quantum Computing, RIKEN, Wako, Saitama 351-0198, Japan. ⁷These authors contributed equally: X. L. He, Yong Lu. ✉e-mail: kdlyong@outlook.com; zrlin@mail.sim.ac.cn

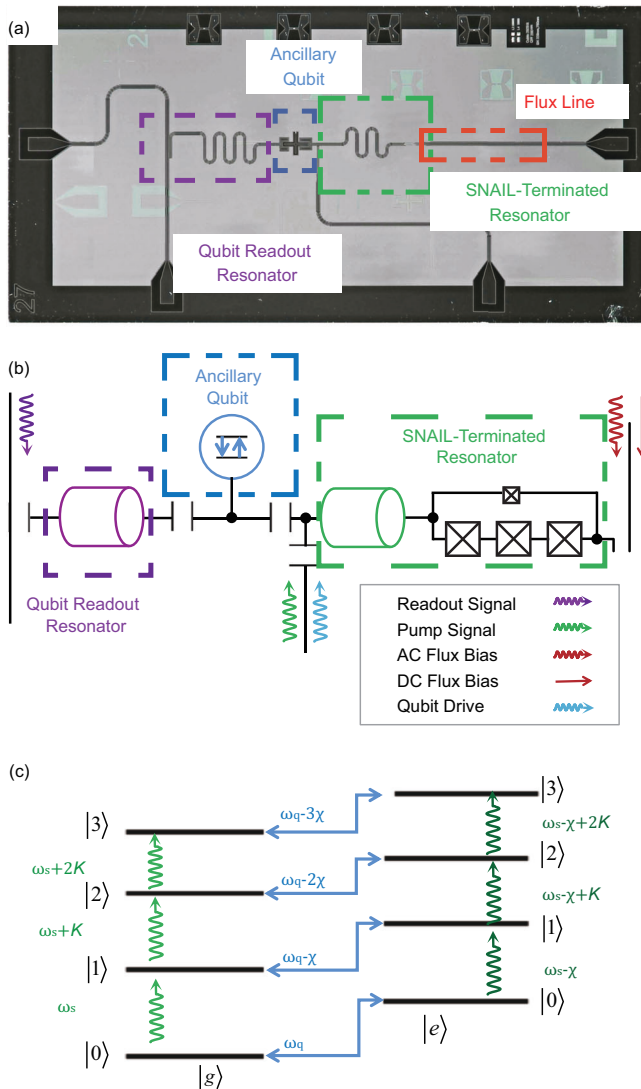


Fig. 1 | Structure of the superconducting circuit. **a** A microscopic photo of the superconducting circuit. An ancillary qubit in the middle is capacitively coupled to both a readout resonator (left) and a SNAIL-terminated resonator (right). **b** Schematic circuit diagram of the system. **c** Energy structure of the dispersively coupled nonlinear resonator and qubit. $|g\rangle$ and $|e\rangle$ are the ground and excited state of qubit respectively. $|0\rangle, |1\rangle, |2\rangle, \dots$ represent the energy levels of the resonator. χ is the dispersive shift.

Results

Design of the quantum circuit

The energy of the SNAIL in our circuit with three big junctions and one smaller junction [Fig. 1c] can be written as²⁹

$$U_{\text{SNAIL}}(\varphi) = -\beta E_J \cos(\varphi) - 3E_J \cos\left(\frac{\varphi_{\text{ext}} - \varphi}{3}\right), \quad (1)$$

where the ratio of the Josephson energies of the small and the big junctions of SNAIL, $\beta \approx 0.095$, the Josephson energy $E_J/h \approx 830\text{GHz}$ ²⁸ (Details in Methods), $\varphi_{\text{ext}} = 2\pi\Phi_{\text{ext}}/\Phi_0$ is the phase induced by the external magnetic flux and φ is the phase difference between two ports of the SNAIL. The Hamiltonian of the SNAIL-terminated resonator is^{10,27,30}:

$$H_{\text{SNAIL-Res}} = \hbar\omega_s a^\dagger a + g_3(a + a^\dagger)^3 + g_4(a + a^\dagger)^4, \quad (2)$$

where ω_s is the resonant frequency of the SNAIL-terminated resonator (the tunable range of $\omega_s/2\pi$ is around 4.08-5.00 GHz in our device). a

(a^\dagger) is the annihilation (creation) operator. $g_3(g_4)$ is the coupling strength for the three (four)-wave mixing.

Including the coupled ancillary transmon qubit, the total effective Hamiltonian of the system in the dispersive regime is given by³¹

$$\begin{aligned} \frac{H_{\text{eff}}}{\hbar} \approx & \omega_s a^\dagger a + K a^{\dagger 2} a^2 + \frac{\omega_q}{2} b^\dagger b \\ & - \frac{\chi}{2} a^\dagger a b^\dagger b - \frac{K_q}{2} b^{\dagger 2} b^2, \end{aligned} \quad (3)$$

where ω_q is the frequency of the ancillary qubit (around 5.09-5.19 GHz). b (b^\dagger) is the lowering (raising) operator for the ancillary qubit. K is the Kerr nonlinearity of the resonator, defined as the frequency shift per photon, $K = K_s + K_{qs}$ with the self-Kerr term $K_s = 12(g_4 - 5g_3^2/\omega_s)$ from the SNAIL element and the cross-Kerr term $K_{qs} = \chi^2/4K_q$ from the qubit with the dispersive shift $\chi/2\pi \approx 3.5 - 18\text{MHz}$ depending on the flux bias [especially $\chi/2\pi \approx 4.35\text{MHz}$ when the external flux $\Phi_{\text{ext}} = 0.4026\Phi_0$ (see Methods)]. The qubit anharmonicity is $K_q/2\pi \approx -420\text{MHz}$. The value of $K_s/2\pi$ can be tuned from negative to positive with a range up to a few MHz [Fig. 2a], whereas the value of $K_{qs}/2\pi$ is always negative on the order of kHz. Therefore, it is possible to cancel the cross-Kerr term from the qubit to obtain $K = 0$ by tuning K_s with the magnetic flux through the SNAIL³², see details in Table 1.

Characterization and manipulation of the nonlinearity

Firstly, we calibrate the values of the Kerr coefficient K [Fig. 2a] precisely with two approaches, namely single-tone and two-tone measurements [Fig. 2b]. For the single-tone measurement, we sweep the frequency of a displacement pulse $D(\alpha)$ followed by a conditional qubit π -pulse, where the qubit is excited only if the SNAIL-terminated resonator is empty (α is the displacement with photon number $N = \alpha^2$). Therefore, we can observe the resonator frequency shift with the photon number inside as shown in Fig. 2c-e. We can extract the Kerr coefficient K by linearly fitting the relationship between the frequency shift and the photon number (see Methods). This method is valid only for a small K so that the total frequency shift is not larger than the pulse linewidth. For a larger K , we switch to perform a two-tone measurement. In this measurement, we regard the nonlinear resonator as a multi-level system with an anharmonicity (similar to a qubit), where we perform Rabi oscillations on the lowest three levels by applying two pulses on the transition $|0\rangle \Rightarrow |1\rangle$ and $|1\rangle \Rightarrow |2\rangle$, respectively. Thus, the anharmonicity, corresponding to the value of K , can be obtained as soon as the resonant frequencies are found (see Methods).

As shown in Fig. 2a, the dynamic range of the Kerr coefficient $K/2\pi$ is approximately from -5MHz to 6MHz which is close to the theoretically simulated result²⁹. Particularly, with flux bias $\Phi_{\text{ext}} = 0.4026\Phi_0$, we find a working point where K is small, $|K/2\pi| < 70\text{kHz}$ from single-tone measurement. The accuracy is limited by the spectroscopic linewidth of the pump pulse. Therefore, the Kerr-induced dynamic evolution is negligible within a time scale on the order of microseconds. At the more accurate Kerr-free point, the nonlinearity from the qubit $K_{qs}/2\pi = \chi^2/4K_q \approx -11\text{kHz}$ can be compensated by K_s , where the dynamic evolution is ideally eliminated. In order to show the merits of preparing the quantum state at the Kerr-free point, as an example, we displace the nonlinear resonator with $\alpha = 1.42$ at $\Phi_{\text{ext}} = 0.4026\Phi_0 (K \approx 0)$ and $\Phi_{\text{ext}} = 0.41\Phi_0 (K/2\pi \approx 0.5\text{MHz})$, respectively. Then, we wait for a time duration Δt before performing the Wigner tomography on the states by taking the parity measurements^{33,34}, where the pulse sequence is shown in Fig. 3a. The results [Fig. 3b-g] clearly illustrate that the quantum states can be preserved well at Kerr-free point whereas the phase of the state collapses when the Kerr nonlinearity is nonzero. Moreover, the frequency shift among energy levels may induce variations in the photon distribution (as what we discussed in the two-tone nonlinearity measurement above). Injection of multiple photons would be much easier

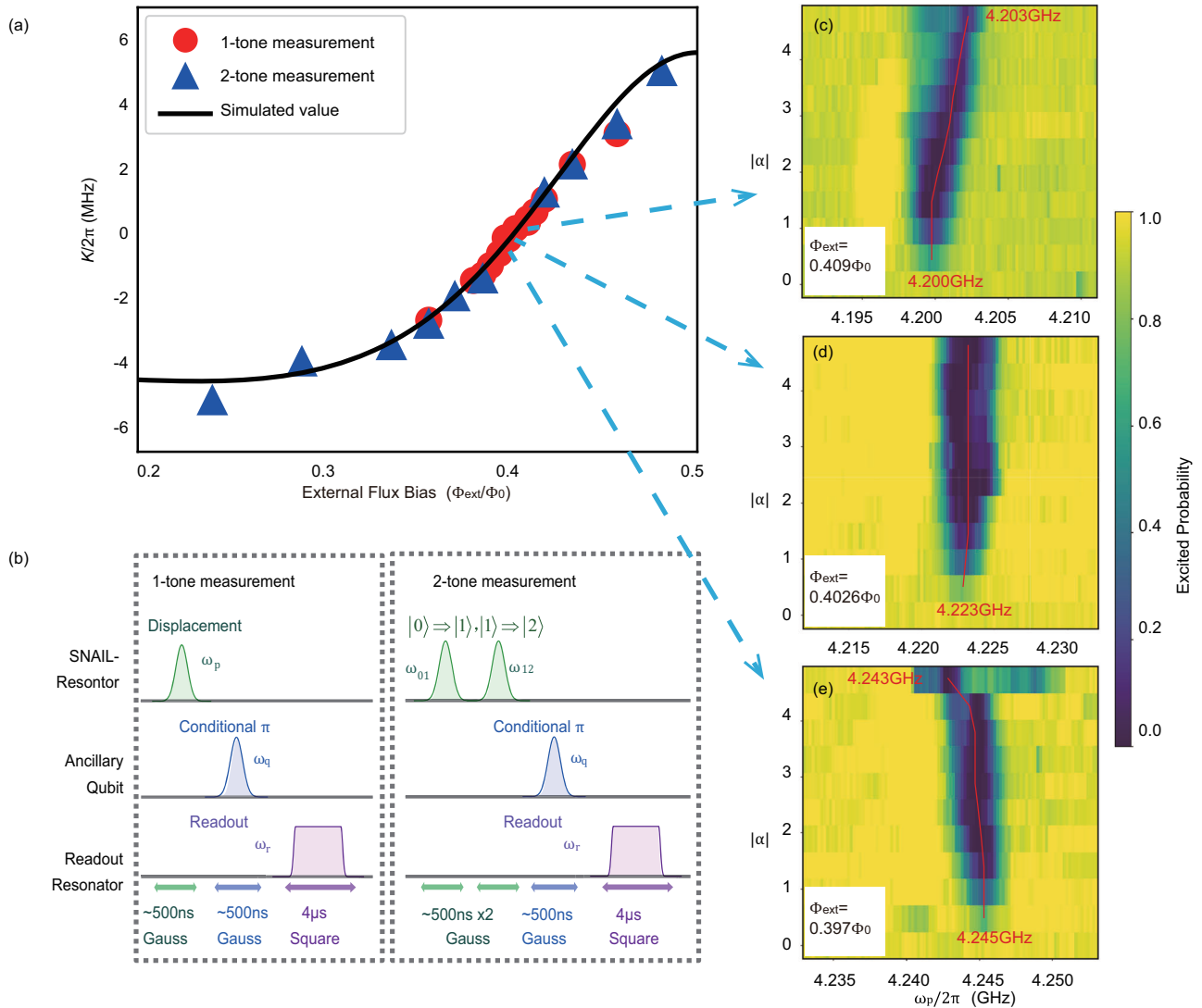


Fig. 2 | Experimental methods to calibrate the tunable nonlinearity of the resonator. **a** Flux bias dependent nonlinearity. The Kerr coefficient K is measured with single-tone and two-tone measurements. **b** Pulse sequences for the single-tone

and two-tone nonlinearity measurements. **c–e** Results of the single-tone measurement near the Kerr-free point. α is the displacement. ω_p is the frequency of the pump pulse to the SNAIL-terminated resonator.

at the Kerr-free point because of the simple spectrum²⁸. As a result, a larger Hilbert space of photons provides us with a larger coding area either for error correction^{9,35,36} or loss suppression²⁶.

Preparation of Schrödinger cat states

Furthermore, the fast tunability of the Kerr coefficient can also be used to generate non-classical quantum states. The Kerr cat qubits²³ with the related error correction methods³⁷ benefiting from Kerr nonlinearity show the potential of dissipation-insensitive and long lifetime quantum computation in a multidimensional Hilbert space.

For example, we consider the Bloch sphere of a Kerr-cat qubit which is constructed with a group of perpendicular states²³:

$$|\varphi_{\pm X}\rangle = |\pm\alpha\rangle, \tag{4}$$

$$|\varphi_{\pm Z}\rangle = |\alpha\rangle \pm |-\alpha\rangle, \tag{5}$$

$$|\varphi_{\pm Y}\rangle = |\alpha\rangle \pm i|-\alpha\rangle, \tag{6}$$

Table 1 | Parameters of the circuit. (ω_{q0} , ω_{s0} , and χ_0 are the values at Kerr-free working point.)

$\omega_q/2\pi$	5.09–5.19 GHz	$\omega_s/2\pi$	4.08–5.00 GHz
$K_q/2\pi$	–420 MHz	$K_s/2\pi$	(–5) –6 MHz
E_J/h	830 GHz	β	0.095
$\chi/2\pi$	3.5–18 MHz	$\omega_{q0}/2\pi$	5.095 GHz
$\omega_{s0}/2\pi$	4.223 GHz	$\chi_0/2\pi$	4.35 MHz

$|\varphi_{\pm X}\rangle = |\pm\alpha\rangle$ are the coherent states generated by pumping our nonlinear resonator with coherent pulses. To prepare the cat states $|\varphi_{\pm Y}\rangle = |\alpha\rangle \pm i|-\alpha\rangle$, the Kerr nonlinearity normally plays an important role^{23,38}. As shown in Fig. 4a, the flux bias pulse (with a pulse width τ) after the first displacement $D(\alpha)$ introduces a flux bias shift, as well as a large Kerr coefficient K . The coherent states evolution under this nonlinear Hamiltonian results in phase shifts among Fock states $|N\rangle$ ($N = 0, 1, 2, \dots$), which means the rotating speed in the phase space is not uniform. Therefore, when we initialize the system with a coherent state $|\alpha\rangle$, the evolution of the field states (during the flux bias pulse in

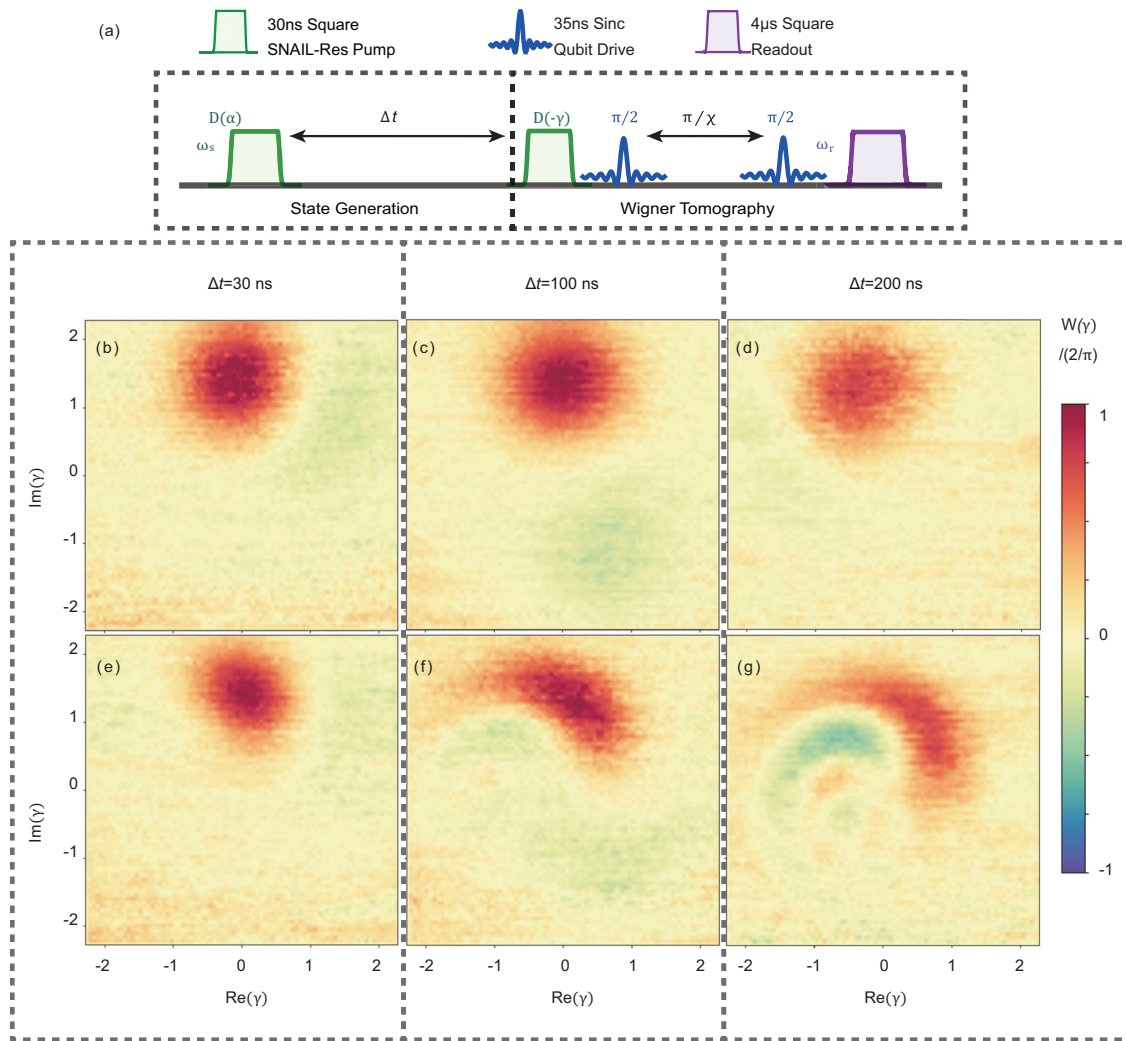


Fig. 3 | Time evolution of a coherent state in the SNAIL-terminated resonator. **a** The pulse sequence where the pulse width of displacement is 30ns, and the time between two displacement pulses is Δt . The experimental Wigner tomography

shows the evolution progress of the coherent states at different time durations as shown in **b–d** at the Kerr-free point and **e–g** with $K/2\pi \approx 0.5\text{MHz}$ where the Kerr effect clearly distorts the state.

Fig. 4a) can be written as²³

$$\begin{aligned} |\Psi(\tau)\rangle &= e^{i\frac{K}{2}(a^\dagger a)^2\tau}|\alpha\rangle \\ &= e^{-|\alpha|^2/2} \sum_N \frac{\alpha^N}{\sqrt{N!}} e^{i\frac{K}{2}N^2\tau}|N\rangle \end{aligned} \quad (7)$$

Under certain circumstances, the m -component cat states can be generated when the nonlinear evolution time $\tau = \tau_0/m$ with $\tau_0 = 2\pi/K$ ($m = 1, 2, \dots$). In particular, when

$$\tau = \pi/K \text{ or } 3\pi/K, \quad (8)$$

the final state is

$$|\Psi(\tau)\rangle = |\alpha\rangle \pm i|-\alpha\rangle. \quad (9)$$

In our experiment, we chose $\alpha = 1.42$ and a flux bias with $K/2\pi = 5.21\text{MHz}$ corresponding to $\tau_0 = 192\text{ns}$. When the pulse width of the flux bias is either $\tau = \tau_0/2 = 96\text{ns}$ or $\tau = 3\tau_0/2 = 288\text{ns}$, we get $|\varphi_{\pm Y}\rangle = |\alpha\rangle \pm i|-\alpha\rangle$. By setting $\tau = \tau_0/3$ (64 ns) and $\tau = \tau_0/4$ (48 ns), we also implement 3- and 4- component cat states which can be used

for quantum error correction^{37,39}. Wigner functions of 2, 3 and 4-component cat states are measured and shown in Fig. 4b–d.

The fidelity of the above Schrödinger’s cat states can be calculated by comparing the measured Wigner function W_{meas} [Fig. 4b–d] with the numerical one W_{cal} [Fig. 4e–g]. The fidelity can be written as⁴⁰

$$F = \pi \int d\gamma^2 W_{\text{meas}}(\gamma) W_{\text{cal}}(\gamma), \quad (10)$$

where γ is the displacement vector, integrated through the whole phase space.

Here, the fidelity F_m of the m -component cat from our measurements is

$$F_2 = 89.1\%, F_3 = 81.3\%, F_4 = 83.15\%. \quad (11)$$

Note that the distortion caused by the imperfect Wigner tomography has not been eliminated. Moreover, the fidelities are currently limited by our device coherent time $1\mu\text{s}$ (see Supplementary Fig. 1). The dominating dephasing source of cat states is the single photon loss in our system (details in Supplementary Fig. 3). Additionally, we need to mention that the ancillary qubit is a nonnegligible source of the collapse and decoherence of the bosonic quantum states. It is therefore

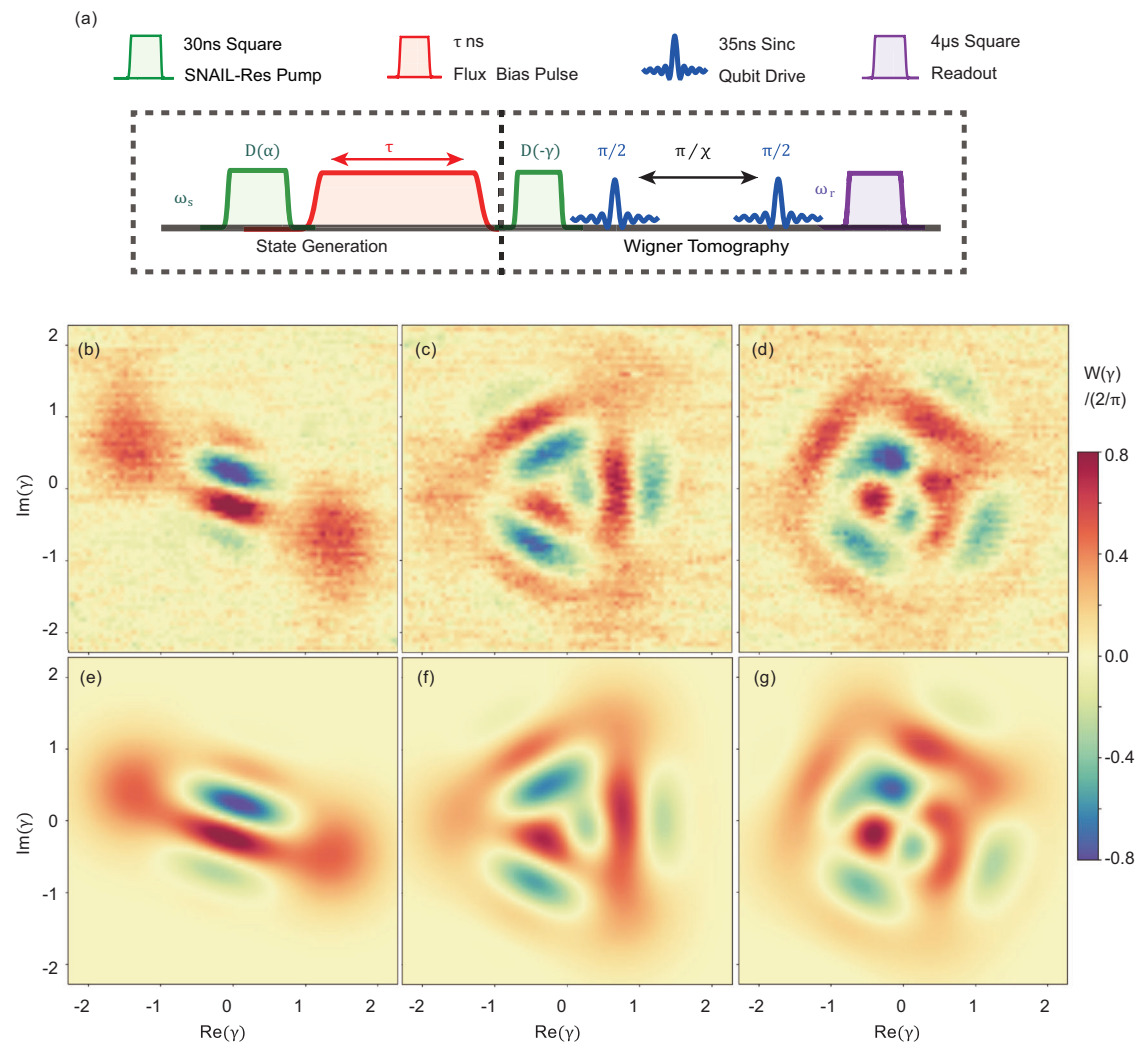


Fig. 4 | Schrödinger cat states generation through the fast modulation of Kerr nonlinearity. **a** Pulse sequence for generating the m -component Poisson distributed cat states. **b–d** Measured Wigner functions of the m -component cat ($m = 2, 3, 4$). **e–g** Numerical Wigner functions of the m -component cat ($m = 2, 3, 4$) obtained through QuTip⁴⁸.

beneficial to reduce the photon loss and the impacts from the qubit (e.g. spectrally isolating the ancillary qubit while not in use).

In previous strategies with a fixed Kerr coefficient^{23,38}, the m -component cat state is stabilized by applying a squeezing drive continuously. However, in our case, the cat states can be maintained in the Kerr-free system passively. Therefore, after the state generation, the system is immediately tuned back to the Kerr-free point, where our resonator can be described by a linear Hamiltonian⁴¹, leading to a better storage and evolution of the cat states within a desirable lifetime (see Methods).

To verify the feasible controllability of our nonlinear resonator, we successfully generate an odd cat state, $|\varphi_{-Z}\rangle = |\alpha\rangle - |-\alpha\rangle$ by following the ancilla-assisted cat preparation method^{42,43}. By using the spectral selectivity and different evolution induced by the dispersive shift, the odd cat state is obtained (details see Supplementary Figure 1). It shows the possibility of constructing a logical qubit with our platform. In conclusion, we have generated nonclassical states through the fast tunable nonlinearity on a SNAIL-terminated resonator where the tunable range is up to 10 MHz. Compared to the cat states in 3D cavities⁴⁴ where the state preparation is based on the ancillary qubit, our method is more straightforward from the fast tuning of the Kerr coefficient of the nonlinear resonator itself. Thus, our scheme is much simpler and has no affect from the imperfect

preparation on the ancillary qubit. Moreover, compared to the two-photon driving strategy^{23,25,38}, the time to prepare the cat states is about $1/K$ in our method, which is several times faster than the adiabatic case³⁸. Meanwhile, by eliminating the Kerr-induced evolution, the states of light can be stored passively without consecutive pump at the Kerr-free point. Finally, our platform is more compact compared to 3D cavities, and shows the capability to integrate more elements. Therefore, our method shows a possibility of the extensible and low-crosstalk bosonic-based quantum computation in the future.

Our method provides an avenue to achieve continuous-variable quantum information processing. It can be used to achieve universal control of bosonic codes. One direct application of our circuitry is constructing hardware-efficient, loss-tolerable quantum computers with error correction codes^{9,44}. Furthermore, networks of coupled resonators can be used to achieve quantum annealing architectures⁴⁵ and quantum simulations such as phase transitions⁴⁶, Gaussian boson sampling⁴⁷, etc.

Methods

Photon number calibration

The photon number in the resonator is measured by the spectroscopy of the ancillary qubit. Here, we pump the resonator with a coherent pulse $D(\alpha)$. As shown in Fig. 5a, due to the dispersive coupling to the qubit, the qubit frequency has a Poisson distribution related to the

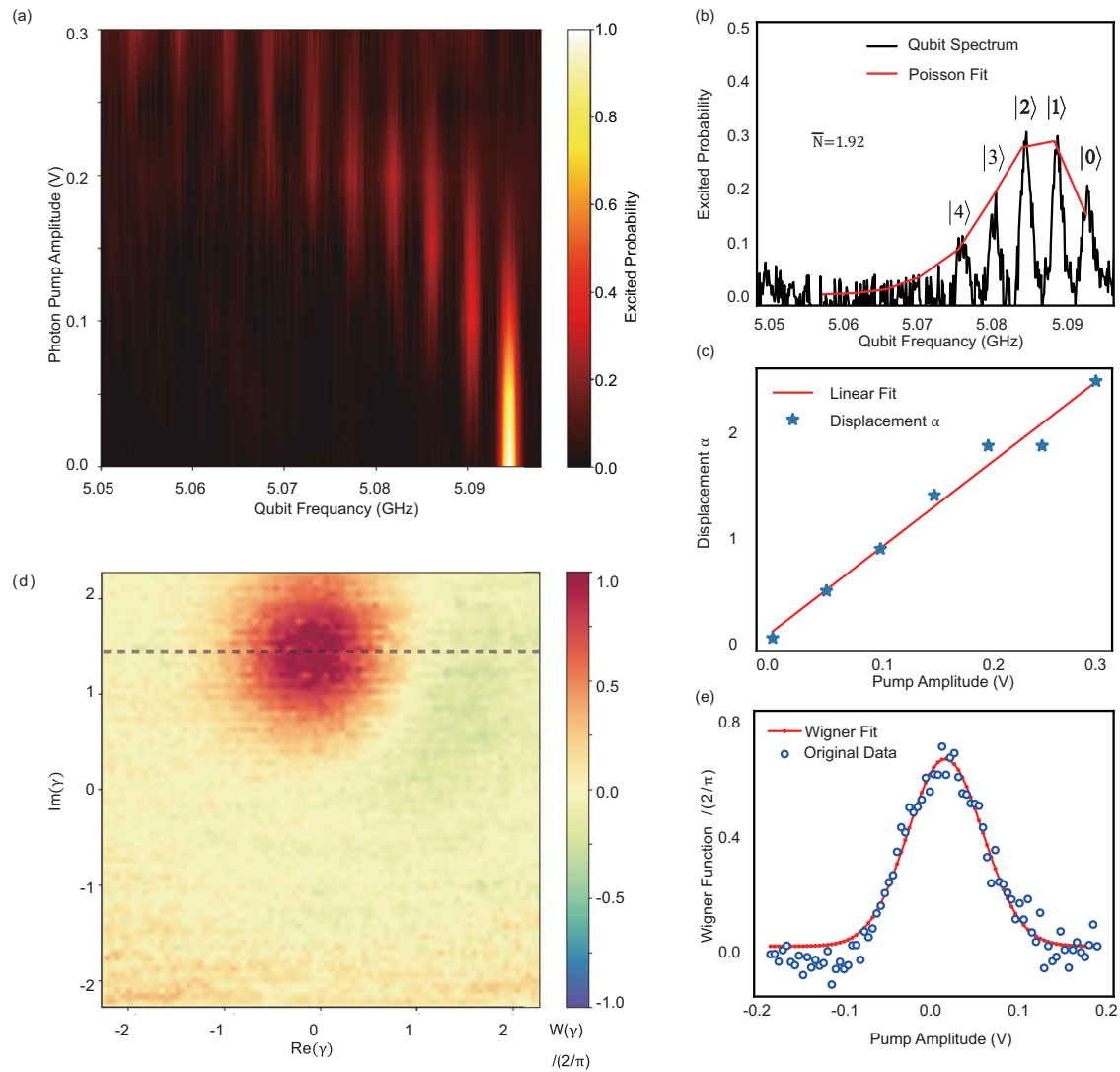


Fig. 5 | Two strategies for photon number calibration. **a** Qubit spectroscopy under different pump pulse amplitudes. **b** Poisson fitting with an average photon number 1.92. **c** Linear relationship between displacement and pump amplitude.

d Wigner function of a coherent state with $\alpha = 1.42$. **e** Fitting of Wigner function (dashed gray line in (d)).

photon pump amplitude V , where the N^{th} peak (away from the native qubit frequency) corresponds to the probability of the Fock state $|N\rangle$ with photon number N . By fitting the multi-peak spectra to a Poisson-distribution function, we can extract the average photon number $\bar{N} = \alpha^2$. Therefore, we can figure out the linear relationship between the photon pump amplitude V and the values of α , namely, $\alpha = G \cdot V$, where G is the scale factor between displacement α and amplitude V .

In addition, to calibrate the photon more precisely under a low photon number ($\bar{N} < 5$), we can also get the relationship $\alpha = G \cdot V$ by fitting the Wigner distribution of the coherent state with [Fig. 5e]:

$$W = \frac{2}{\pi} \exp(-2(\alpha - \alpha_0)^2) = \frac{2}{\pi} \exp(-2(G \cdot V - \alpha_0)^2), \quad (12)$$

where α_0 is the initial displacement.

These relationships are used for the nonlinearity, Wigner function and lifetime measurements discussed in the main text. However, because of the flux-dependent nonlinearity, the photon-number distribution does not satisfy Poisson function when the frequency shift $N \cdot K$ is comparable with the linewidth of the pump

pulse (≈ 2 MHz for the 500 ns pump pulse). The photon number calibration methods above are therefore only available for $\Phi - 0.4\Phi_0$ with $|K/2\pi| < 2$ MHz.

Nonlinearity characterization

The Hamiltonian of the SNAIL element with three large Josephson junctions (with Josephson energy E_J) and one smaller junction (βE_J) can be written as (same as Eq. (1)):

$$U_{\text{SNAIL}}(\varphi_s) = -\beta E_J \cos(\varphi_s) - 3E_J \cos\left(\frac{\varphi_{\text{ext}} - \varphi_s}{3}\right), \quad (13)$$

where φ_{ext} is the external magnetic flux induced phase through the SNAIL loop, φ_s is the phase different between the two ports of SNAIL. Coupled with a resonator (represented by capacity C and inductance L):

$$H = C \frac{\Phi_0^2}{2} \dot{\varphi}^2 + U(\varphi, \varphi_s), \quad (14)$$

$$U(\varphi, \varphi_s) = \frac{1}{2} E_L (\varphi - \varphi_s)^2 + U_{\text{SNAIL}}(\varphi_s), \quad (15)$$

where φ is the mode canonical phase coordinate and $E_L = \Phi_0^2/L$ is the inductive energy. After Taylor expansion around the minimum

point of potential U , the Hamiltonian of second quantization is^{28,29}

$$H_{\text{SNAIL-Res}} = \hbar\omega_s a^\dagger a + g_3(a + a^\dagger)^3 + g_4(a + a^\dagger)^4, \quad (16)$$

where

$$\hbar\omega_s = \sqrt{8E_C E_J c_2}, \quad (17)$$

$$\hbar g_3 = c_3 \sqrt{E_C \hbar\omega_s} / 6c_2, \quad (18)$$

$$\hbar g_4 = c_4 E_C / 12c_2, \quad (19)$$

$$c_j = \frac{1}{E_J} \left. \frac{d^j U}{d\varphi^j} \right|_{\varphi_m}, \quad (20)$$

$$E_C = e^2 / 2C. \quad (21)$$

The energy level n is:

$$E_n / \hbar = n\omega_s + 6(g_4 - 5g_3^2 / \omega_s)n(n+1). \quad (22)$$

Thus, the Kerr coefficient of SNAIL-terminated resonator can be written as

$$\hbar K = \frac{d^2 E_n}{dn^2} = 12\hbar \left(g_4 - \frac{5g_3^2}{\omega_s} \right). \quad (23)$$

The design parameters β and E_J , also the relationship between injected current and flux φ_{ext} can be extracted by fitting the flux modulation of the SNAIL-terminated resonator frequency (Fig. 6) with Eq. (22)²⁸.

We developed two methods for the Kerr coefficient characterization, namely, single-tone and two-tone measurements. The single-tone measurement is only suitable for smaller Kerr coefficient (e.g. $|K/2\pi| < 2$ MHz). To contrast, larger K brings more frequency shift with a similar photon number. When the frequency shift is larger than the linewidth of the single pulse, the nonlinearity can be measured by the two-tone method.

In a single-tone measurement, in order to keep the frequency sensitivity, we choose a relatively long pulse with a pulse length up to 500 ns, then we sweep the pulse frequency with following a conditional π -pulse which can excite the qubit only if the cavity is empty. Therefore, it can be regarded as a photon probe. With different pump powers, we can see the shift of resonant frequency Δf which obeys:

$$K/2\pi = f_N - f_{N-1}, \quad (24)$$

$$K/2\pi = \Delta f / \bar{N}, \quad (25)$$

where \bar{N} is the average photon number. For example, in Fig. 2c, we see the frequency shift with different displacement (i.e. pump amplitude). By linearly fitting the relationship of the frequency shift and the average photon number, we get the Kerr coefficient [Fig. 7a]. If K is too large ($|K/2\pi| > 2$ MHz), however, it is not possible to cover the frequency range with a single tone. Then, we treat the SNAIL-terminated resonator as a three level system with an anharmonicity K . To verify it, Rabi oscillations between energy levels ($|0\rangle \leftrightarrow |1\rangle$ and $|1\rangle \leftrightarrow |2\rangle$) are measured [Fig. 7b]. Here, the conditional qubit π pulse is also modified to be only valid for $|0\rangle, |1\rangle$ or $|2\rangle$, respectively. Thus, K is represented by the frequency difference of the first two pulses as

$$K/2\pi = f(|1\rangle \leftrightarrow |2\rangle) - f(|0\rangle \leftrightarrow |1\rangle). \quad (26)$$

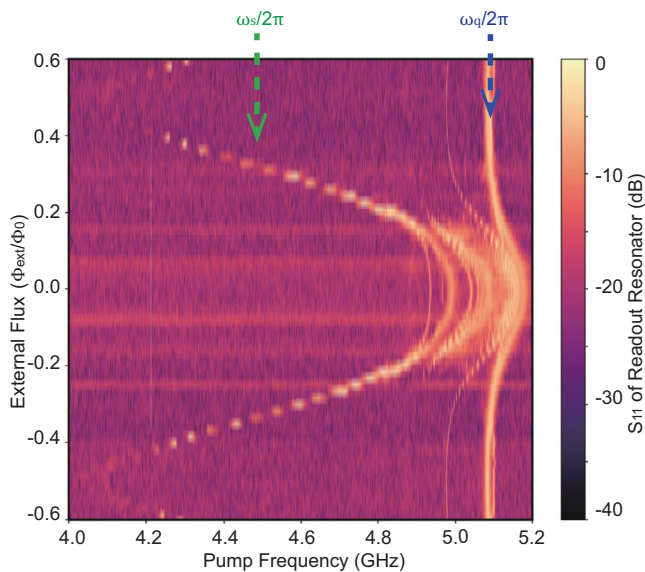


Fig. 6 | Flux modulated spectrum. The frequencies of the SNAIL-terminated resonator and ancillary qubit are obtained by the reflection coefficient measurement on the readout resonator with different pump frequency.

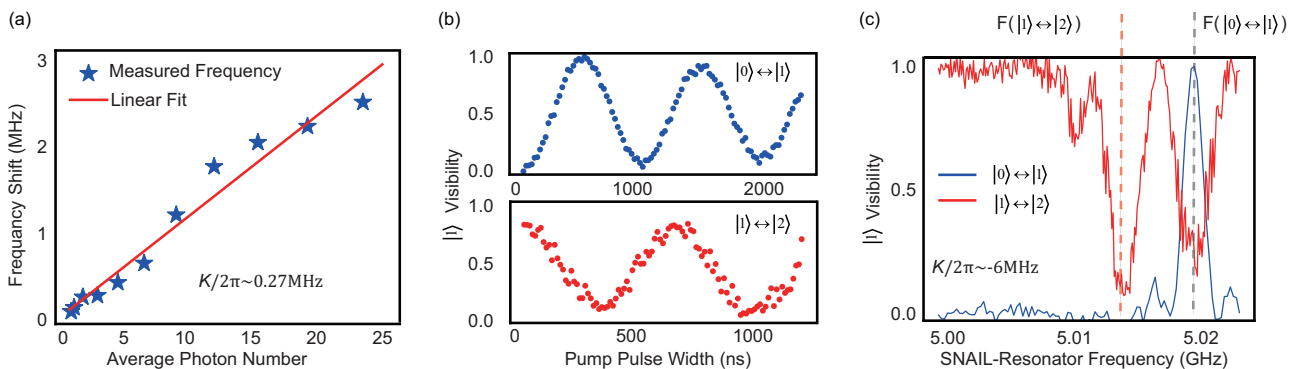


Fig. 7 | Experimental results of 1-tone and 2-tone nonlinearity measurement. **a** Relationship between the frequency shift and the photon number in 1-tone measurement with external flux $\Phi_{\text{ext}} = 0.409\Phi_0$. **b** Rabi oscillation between the

Fock states ($|0\rangle \leftrightarrow |1\rangle$ and $|1\rangle \leftrightarrow |2\rangle$). **c** Frequency scan of the SNAIL-terminated resonator under a 2-tone measurement with a conditional π pulse for $|1\rangle$ ($\Phi_{\text{ext}} = 0.24\Phi_0$).

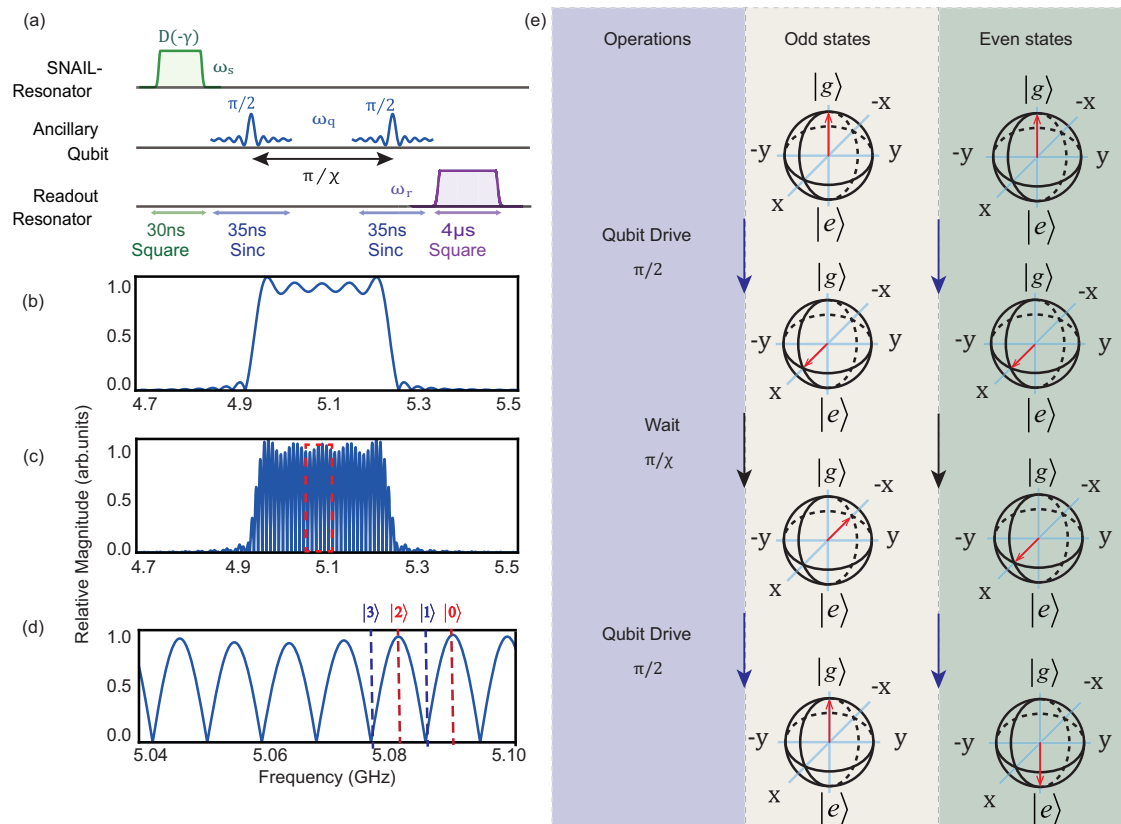


Fig. 8 | Wigner tomography. **a** Pulse sequence for Wigner tomography. **b** Frequency spectrum of a sinc shaped pulse. **c** Frequency spectrum of two sinc pulses with a time spacing π/χ . **d** Enlarged view of (c). **e** Bloch sphere of the ancillary qubit during the cat state Wigner tomography.

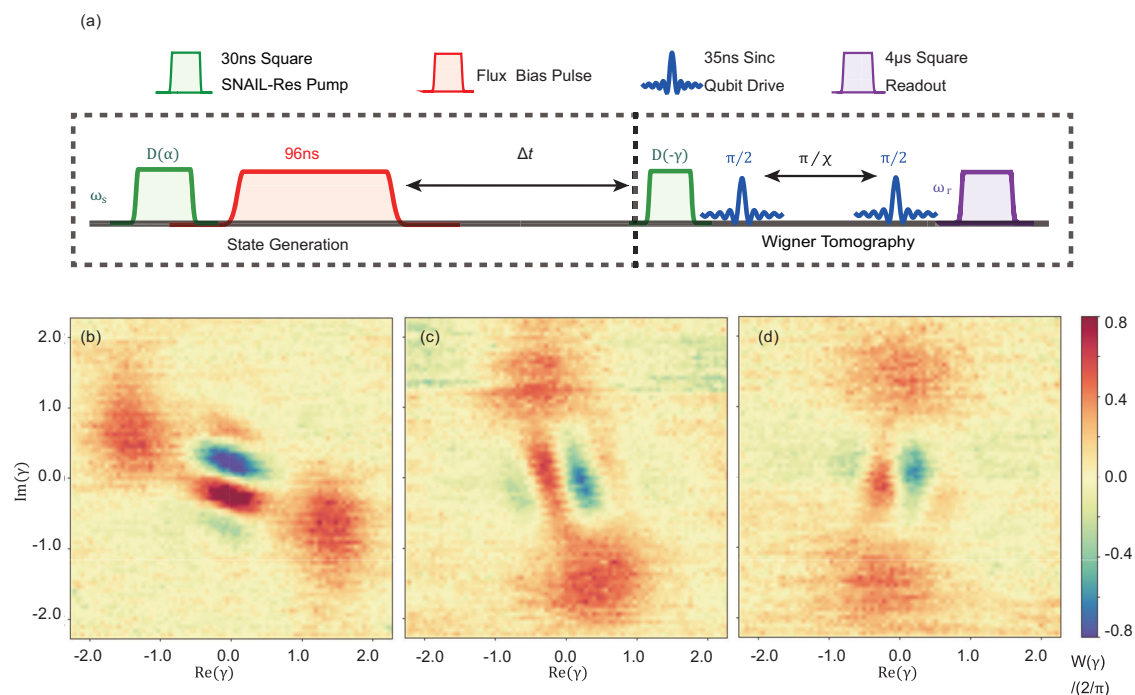


Fig. 9 | Cat states generation and preservation. **a** Pulse sequence for 2-component cat $|\alpha\rangle \pm i|\alpha\rangle$ preparation. After preparation, the states are measured after $\Delta t =$ **(b)** 0 ns, **(c)** 100 ns, **(d)** 200 ns.

The measurement results from single-tone and two-tone methods agree with the theoretical calculation very well [Fig. 2a].

Wigner tomography

The Wigner function of the states is obtained by the parity measurement. For definition, the Wigner function can be described as

$$W(\gamma) = \frac{2}{\pi} \text{Tr}[D(-\gamma)\rho D(\gamma)P], \quad (27)$$

$$P = e^{i\pi a^\dagger a} = (-1)^N, \quad (28)$$

By applying a displacement $D(-\gamma)$ to a density operator ρ , we get a new state with density operator:

$$\rho' = D(-\gamma)\rho D(\gamma). \quad (29)$$

Thus, the Wigner function $W(\gamma)$ is proportional to the average of parity operator P which can be measured with the sequence in Fig. 8a. Here, we apply two $\pi/2$ pulses to the ancillary qubit. With a time spacing π/χ between two pulses, this sequence can be treated as a parity measurement where the state of qubit $|g\rangle$ ($|e\rangle$) corresponds to $P = -1$ (1). The mechanism can be described in the qubit Bloch sphere [Fig. 8e] and signal spectrum [Fig. 8b–d]. The sequence to qubit is π (2π) pulse if photon number N is even (odd). Considering the frequency shift of qubit, we employ a function of $\text{sinc}(t) = \sin(t)/t$ to cover a larger spectrum range uniformly.

States preservation

After the process of states generation, the cat states are preserved by turning the flux bias off. Here, the Wigner functions are measured after a certain evolution time Δt . As shown in Fig. 9b–d, the Kerr-induced evolution is ideally prevented, the fidelity of 2-component cat ($|\alpha\rangle \pm i|\alpha\rangle$) state is 89.1%, 81.9% and 75.8% after (0, 100, 200 ns).

Data availability

The data that support the findings of this study are available in figshare [<https://doi.org/10.6084/m9.figshare.23694369>].

References

- Arute, F. et al. Quantum supremacy using a programmable superconducting processor. *Nature* **574**, 505–510 (2019).
- Jaksch, D. et al. Fast quantum gates for neutral atoms. *Phys. Rev. Lett.* **85**, 2208 (2000).
- Monroe, C. & Kim, J. Scaling the ion trap quantum processor. *Science* **339**, 1164–1169 (2013).
- Bruzewicz, C. D. et al. Trapped-ion quantum computing: progress and challenges. *Appl. Phys. Rev.* **6**, 021314 (2019).
- Kjaergaard, M. et al. Superconducting qubits: Current state of play. *Annu. Rev. Condens. Matter Phys.* **11**, 369–395 (2020).
- Gong, M. et al. Quantum walks on a programmable two-dimensional 62-qubit superconducting processor. *Science* **372**, 948–952 (2021).
- Fowler, A. G. et al. Surface codes: Towards practical large-scale quantum computation. *Phys. Rev. A* **86**, 032324 (2012).
- Vlastakis, B. et al. Deterministically encoding quantum information using 100-photon Schrödinger cat states. *Science* **342**, 607–610 (2013).
- Campagne-Ibarcq, P. et al. Quantum error correction of a qubit encoded in grid states of an oscillator. *Nature* **584**, 368–372 (2020).
- Hillmann, T. et al. Universal gate set for continuous-variable quantum computation with microwave circuits. *Phys. Rev. Lett.* **125**, 160501 (2020).
- Altman, E. et al. Quantum simulators: Architectures and opportunities. *PRX Quantum* **2**, 017003 (2021).
- Sivak, V. V. et al. Real-time quantum error correction beyond break-even. *Nature* **616**(mar), 50–55 (2023).
- Ni, Z. et al. Beating the break-even point with a discrete-variable-encoded logical qubit. *Nature* **616**(mar), 56–60 (2023).
- Hofheinz, M. et al. Synthesizing arbitrary quantum states in a superconducting resonator. *Nature* **459**, 546–549 (2009).
- Leibfried, D. et al. Experimental determination of the motional quantum state of a trapped atom. *Phys. Rev. Lett.* **77**, 4281 (1996).
- Chamberland, C. et al. Building a fault-tolerant quantum computer using concatenated cat codes. *PRX Quantum* **3**, 010329 (2022).
- Ma, Y. et al. Error-transparent operations on a logical qubit protected by quantum error correction. *Nat. Phys.* **16**, 827–831 (2020).
- Gottesman, D., Kitaev, A. & Preskill, J. Encoding a qubit in an oscillator. *Phys. Rev. A* **64**, 012310 (2001).
- Ma, Wen-Long et al. Quantum control of bosonic modes with superconducting circuits. *Sci. Bull.* **66**, 1789–1805 (2021).
- Lloyd, S. & Braunstein, S. L. Quantum computation over continuous variables. *Phys. Rev. Lett.* **82**, 1784 (1999).
- Kirchmair, G. et al. Observation of quantum state collapse and revival due to the single-photon Kerr effect. *Nature* **495**, 205–209 (2013).
- Leghtas, Z. et al. Confining the state of light to a quantum manifold by engineered two-photon loss. *Science* **347**, 853–857 (2015).
- Grimm, A. et al. Stabilization and operation of a Kerr-cat qubit. *Nature* **584**, 205–209 (2020).
- Eickbusch, A. et al. Fast universal control of an oscillator with weak dispersive coupling to a qubit. *Nat. Phys.* **18**(oct), 1464–1469 (2022).
- Lescanne, Raphaël et al. Exponential suppression of bit-flips in a qubit encoded in an oscillator. *Nat. Phys.* **16**, 509–513 (2020).
- Berdou, C. et al. One hundred second bit-flip time in a two-photon dissipative oscillator. *PRX Quantum* **4**, 020350 (2023).
- Frattini, N. E. et al. 3-wave mixing Josephson dipole element. *Appl. Phys. Lett.* **110**, 222603 (2017).
- Lu, Y. et al. Resolving Fock states near the Kerr-free point of a superconducting resonator. Preprint at <https://arxiv.org/abs/2210.09718> (2022).
- Frattini, N. E. et al. Optimizing the nonlinearity and dissipation of a snail parametric amplifier for dynamic range. *Phys. Rev. Appl.* **10**, 054020 (2018).
- Dykman, M. *Fluctuating Nonlinear Oscillators: From Nanomechanics To Quantum Superconducting Circuits* (Oxford University Press, 2012).
- Noguchi, A. et al. Fast parametric two-qubit gates with suppressed residual interaction using the second-order nonlinearity of a cubic transmon. *Phys. Rev. A* **102**, 062408 (2020).
- Yamaji, T. et al. Spectroscopic observation of the crossover from a classical Duffing oscillator to a Kerr parametric oscillator. *Phys. Rev. A* **105**, 023519 (2022).
- Deleglise, S. et al. Reconstruction of non-classical cavity field states with snapshots of their decoherence. *Nature* **455**, 510–514 (2008).
- von Lüpke, U. et al. Parity measurement in the strong dispersive regime of circuit quantum acoustodynamics. *Nat. Phys.* **18**, 794–799 (2022).
- Kudra, M. et al. Robust preparation of Wigner-negative states with optimized SNAP-displacement sequences. *PRX Quantum* **3**, 030301 (2022).
- Livingston, W. P. et al. Experimental demonstration of continuous quantum error correction. *Nat. Commun.* **13**, 1–7 (2022).
- Ofek, N. et al. Extending the lifetime of a quantum bit with error correction in superconducting circuits. *Nature* **536**, 441–445 (2016).
- Puri, S., Boutin, S. & Blais, A. Engineering the quantum states of light in a Kerr-nonlinear resonator by two-photon driving. *npj Quantum Inf.* **3**, 1–7 (2017).

39. Bergmann, M. & van Loock, P. Quantum error correction against photon loss using multicomponent cat states. *Phys. Rev. A* **94**, 042332 (2016).
40. Chizhov, A. V., Knöll, L. & Welsch, D.-G. Continuous-variable quantum teleportation through lossy channels. *Phys. Rev. A* **65**, 022310 (2002).
41. Hillmann, T. & Quijandria, F. Designing Kerr interactions for Quantum Information Processing via Counterrotating Terms of Asymmetric Josephson-Junction Loops. *Phys. Rev. Appl.* **17**, 064018 (2022).
42. Haroche, S. & Raimond, J. *Exploring the Quantum: Atoms, Cavities, and Photons* (Oxford University Press, 2006).
43. Savage, C. M., Braunstein, S. L. & Walls, D. F. Macroscopic quantum superpositions by means of single-atom dispersion. *Opt. Lett.* **15**, 628–630 (1990).
44. Terhal, B. M., Conrad, J. & Vuillot, C. Towards scalable bosonic quantum error correction. *Quantum Sci. Technol.* **5**, 043001 (2020).
45. Lechner, W., Hauke, P. & Zoller, P. A quantum annealing architecture with all-to-all connectivity from local interactions. *Sci. Adv.* **1**, e1500838 (2015).
46. Dykman, M. I. et al. Interaction-induced time-symmetry breaking in driven quantum oscillators. *Phys. Rev. B* **98**, 195444 (2018).
47. Arrazola, J. M. et al. Quantum circuits with many photons on a programmable nanophotonic chip. *Nature* **591**, 54–60 (2021).
48. Barends, R. et al. Superconducting quantum circuits at the surface code threshold for fault tolerance. *Nature* **508**(Apr), 500–3 (2014).

Acknowledgements

The authors acknowledge the use of the Nanofabrication Laboratory (NFL) at Chalmers. We wish to express our gratitude to Xiaoming Xie, Lars Jönsson, Fernando Quijandria, Timo Hillmann, and Hang-Xi Li for help. This work is supported in part by the Shanghai Technology Innovation Action Plan Integrated Circuit Technology Support Program (No. 22DZ1100200), the National Natural Science Foundation of China (No. 92065116), Strategic Priority Research Program of the Chinese Academy of Sciences (Grant No. XDA18000000), and the Key-Area Research and Development Program of Guangdong Province, China (No. 2020B0303030002). Y.L. and P.D. acknowledge support from the Knut and Alice Wallenberg Foundation via the Wallenberg Center for Quantum Technology (WACQT) and from the Swedish Research Council (Grant number 2015-00152).

Author contributions

X.L.H. and Z.R.L. conceived the experiment. X.L.H. performed the experiments and analyzed the data. Y.L. triggered the project, designed,

simulated, fabricated the device and helped with the measurement and analysis. D.Q.B. provided the theoretical support. X.L.H. wrote the manuscript together with Y.L. and Z.R.L. H.X., W.B.J., and X.L.H. built up the measurement system. A.F.R. helped with the development of the fabrication recipe. Z.W., P.D., and J.S.T. contributed to discussions of the results. All authors contributed to revising and proofreading of the manuscript. Z.R.L. supervised the project.

Competing interests

The authors declare no competing interests.

Additional information

Supplementary information The online version contains supplementary material available at <https://doi.org/10.1038/s41467-023-42057-0>.

Correspondence and requests for materials should be addressed to Yong Lu or Z. R. Lin.

Peer review information *Nature Communications* thanks the anonymous reviewer(s) for their contribution to the peer review of this work. A peer review file is available.

Reprints and permissions information is available at <http://www.nature.com/reprints>

Publisher's note Springer Nature remains neutral with regard to jurisdictional claims in published maps and institutional affiliations.

Open Access This article is licensed under a Creative Commons Attribution 4.0 International License, which permits use, sharing, adaptation, distribution and reproduction in any medium or format, as long as you give appropriate credit to the original author(s) and the source, provide a link to the Creative Commons licence, and indicate if changes were made. The images or other third party material in this article are included in the article's Creative Commons licence, unless indicated otherwise in a credit line to the material. If material is not included in the article's Creative Commons licence and your intended use is not permitted by statutory regulation or exceeds the permitted use, you will need to obtain permission directly from the copyright holder. To view a copy of this licence, visit <http://creativecommons.org/licenses/by/4.0/>.

© The Author(s) 2023